



# Chemical element mapping by x-ray computational ghost fluorescence

YISHAY KLEIN,  OR SEFI,  HILA SCHWARTZ, AND SHARON SHWARTZ\*

Physics Department and Institute of Nanotechnology and Advanced Materials, Bar Ilan University, Ramat Gan, 52900, Israel

\*Corresponding author: sharon.shwartz@biu.ac.il

Received 26 August 2021; revised 7 December 2021; accepted 7 December 2021; published 13 January 2022

**Chemical element mapping is an imaging tool that provides essential information about composite materials, and it is crucial for a broad range of fields ranging from fundamental science to numerous applications. Methods that exploit x-ray fluorescence are very advantageous and are widely used, but require focusing of the input beam and raster scanning of the sample. Thus, the methods are slow and exhibit limited resolution due to focusing challenges. Here, we demonstrate an x-ray fluorescence method based on computational ghost imaging that overcomes those limitations since it does not require focusing and show that when it is combined with compressed sensing the total measurement time can be significantly reduced. Our method opens the possibility to significantly enhance the resolution of chemical element maps and to extend the applicability of x-ray fluorescence inspection to new fields where the measurement time is a critical parameter.** © 2022 Optical Society of America under the terms of the [OSA Open Access Publishing Agreement](https://doi.org/10.1364/OPTICA.441682)

<https://doi.org/10.1364/OPTICA.441682>

## 1. INTRODUCTION

x-ray fluorescence (XRF) is a powerful method to identify and map the chemical compositions of samples with intriguing applications that are exploited in a broad range of fields from fundamental science to industry and cultural heritage. Examples for scientific disciplines where XRF plays a prominent role include materials science, electrochemistry [1], biology [2], paleontology [3], and archaeology [4]. Industrial applications include, for example, metal analyzers for small parts that are produced by the automotive and aerospace industries [5]. In cultural heritage, XRF is very useful in providing information on the hidden layers of famous paintings [6].

The basic principle of XRF is simple and is based on the x-ray fluorescence process in which x-ray radiation is used to excite core electrons in the sample. When the core electrons are excited or ejected from the inner shells of the atoms, holes are formed in those shells. The electrons can return to their ground state or outer electrons can fill the holes leading to the emission of x-ray radiation at photon energies that correspond to the characteristic atomic lines. The spectrum of the emitted radiation (the fluorescence spectrum) is detected and analyzed, and since each chemical element has unique emission lines, the fluorescence spectrum is used to characterize the elemental composition of the sample. The detection can be done by energy-resolving detectors that are simple to use and available components with sufficient energy resolution.

In its simplest form, XRF provides no spatial information since the detector collects the radiation from large areas; in recent decades, however, spatially resolved XRF techniques have been developed and their advent opens appealing opportunities in many fields [1,3,4,6]. However, the main challenge for spatially resolved

XRF measurements is that, in contrast to transmission measurements, the fluorescence is nondirectional, which means that the application of pixelated detectors is a great challenge. Instead, in most cases, 2D chemical maps are reconstructed by focusing the impinging beam and raster-scanning the sample. With this procedure, the spatial information is retrieved since at each measurement point only a small portion of the sample is irradiated and the resolution is determined by the spot size of the input beam [7]. When the spot size is on the order of several microns, the method is called micro-XRF. Extensions to 3D are also possible by either computed tomography [8,9] or confocal x-ray microscopy [10,11].

Despite being very successful and widely used, XRF faces two major challenges that hamper its performance and the extension of its applicability to further disciplines: (1) focusing of x-ray radiation is difficult, especially at high photon energies, so the ability to use small spot sizes in a broad photon energy range is unique to very few synchrotron beamlines and x-ray free electron lasers [7]. To date, the highest resolution achieved with tabletop sources is several microns [12]. However, it is achievable only in a very limited range of photon energies and at the expense of a significant loss of the input flux. (2) In almost all practical implementations of micro-XRF, the spatial information is obtained by raster scanning. This is a very slow process since the scan is done over every point of sample. For large samples and for 3D imaging, the measurement time is several days.

We note reports on several methods for full-field XRF, which are implemented by photon-energy-resolving pixelated detectors, with capabilities to provide 2D chemical maps in a single frame [13–16]. These techniques are performed by using either simple [13,16] or coded [14,15] apertures in front of the pixelated

detector to address the challenge of the blurring due to the non-directionality of the fluorescence. However, the spatial resolution and the field of view (for a fixed number of pixels) are limited [13–15]. In addition, because the quantum efficiency of the detectors drops very quickly at photon energies higher than 20 keV, there are inflexible constraints on the distance between the sample and the detector, and the measurements cannot provide 3D information without additional lenses [16], which introduces severe challenges. Another approach to reduce the duration of the XRF measurements is based on scanning procedures [17,18] and information that is obtained from the sample during the scan to improve the scanning efficiency [19]. This is a very interesting direction, but the setup is different and the focusing of the input x-ray beam is still required.

Here, we propose and demonstrate a proof-of-principle experiment for what we believe, to the best of our knowledge, is a new and fast, XRF approach with potentially high spatial resolution that solves those challenges by using structured illumination and correlation. The main advantages of our approach are that it does not require focusing and that the measurement time can be significantly reduced by using compressed sensing (CS) or artificial intelligence (AI) algorithms since our method requires a significantly smaller number of measurement points compared to standard techniques.

Our approach that we denote as x-ray computational ghost fluorescence (GF) is related to the computational ghost imaging (GI) approach proposed by Shapiro in 2008 [20]. While the initial motivation of the computational GI approach was to show that quantum correlations are not essential for GI, it evolved to many interesting directions with intriguing potential applications and has been investigated extensively in a broad range of wavelengths [20–35] from radio waves [23] to X-rays [26,29–32], and even with neutrons [36], and electrons [37]. Computational GI can be used to reconstruct 2D and 3D images [28] and, by using CS [35] or AI [22], the measurement time can be significantly reduced. While several schemes for GI have been demonstrated with X-rays [26,29–32,38–41], in the present work we replace the measurement of the transmission or reflection of the object by the measurement of the x-ray fluorescence, which carries the information on the chemical elements; hence, we can use it for chemical mapping.

We note that the GI approach has been used in the visible range for the measurement of the fluorescence [27,33,34]. However, long wavelength fluorescence measurements are not element specific and, in contrast to our method, cannot be used for chemical element mapping. Moreover, the implementation of GI for XRF, where the main alternative is raster scanning, expresses the strengths of the GI approach, which are the ability to provide spatial information without lenses or mirrors and the natural suitability for compressive measurements, which can be used to reduce the measurement time [42].

## 2. IMAGE RECONSTRUCTION PROCEDURE

Our procedure relies on a two-step approach for the implementation of computational GI [32]. A flowchart that illustrates the procedure is shown in Fig. 1(a). In both steps, the x-ray beam irradiates a mask with inhomogeneous transmission that induces intensity fluctuations in the beam. The goal of Step I is to measure the intensity fluctuations that the mask introduces at the plane of the sample for each of the realizations that we use in Step II. As we

illustrate in Fig. 1(b), this is done in the absence of the object and by mounting a pixelated detector at the plane at which we mount the object in Step II. In Step II, which is depicted in Fig. 1(c), we remove the pixelated detector, insert the object, scan the mask at the same positions as in Step I, and measure the x-ray fluorescence with two photon-energy-resolving silicon drift detectors (SDDs) located at two different positions, as shown in Fig. 1(c). We denote the detector that is located upstream the sample as detector  $R$  and the detector located downstream from the sample as detector  $T$ . We use two detectors to show that the chemical map can be reconstructed by mounting the detector at any direction around the sample and each of the maps is reconstructed using the data from a single SDD.

After completing the measurements for the entire set of realizations, we obtained two sets of data. One contains the patterns of the mask (measured in Step I) and the other contains the corresponding intensities for each of the fluorescence emission lines (measured in Step II). To reconstruct each shape of the emitters, we separately exploit the following reconstruction procedure for each chemical element. We represent the spatial distribution of each chemical element by a vector  $\mathbf{x}$ . Another vector  $\mathbf{T}$ , which includes  $n$  realizations, represents the intensities of the corresponding emission lines measured by the each of the SDDs. The mask patterns are represented by the matrix  $\mathbf{A}$ , for which every row is a single realization. The vector  $\mathbf{T}$  is equal to the product of the matrix  $\mathbf{A}$  and the vector  $\mathbf{x}$ :

$$\mathbf{Ax} = \mathbf{T}. \quad (1)$$

To find the vector  $\mathbf{x}$  with a minimal number of realizations, and consequently to reduce the measurement time, we used the CS approach, which uses a priori knowledge on the structure of the image. We used the protocol of “total variation minimization by augmented Lagrangian and alternating direction algorithms” (TVL3) [43]. The basic concept of the protocol is that the gradient of many objects in nature can be represented by a sparse matrix. For each chemical element, the vector  $\mathbf{x}$  is reconstructed by minimizing the augmented Lagrangian:

$$\min_{\mathbf{x}} \sum_{i=1}^m \|D_i \mathbf{x}\|_2 + \frac{\mu}{2} \|\mathbf{Ax} - \mathbf{T}\|_2^2 \text{ s.t } \mathbf{x} \geq 0, \quad (2)$$

with respect to the  $L_2$  norm. Here,  $D_i \mathbf{x}$  is the  $i^{\text{th}}$  component of the discrete gradient of the vector  $\mathbf{x}$ , and  $\mu$  is the penalty parameter of the model. Here, we set  $\mu = 2^9$ ). After we reconstruct the image for each of the chemical elements, we overlay the images to reconstruct the chemical element map.

## 3. RESULTS

The source we used in this experiment was a rotating copper anode and the mask was a sandpaper with an average feature size of about 40  $\mu\text{m}$ . Since we used a collimator before the mask, the intensity patterns we measured in Step I [see Fig. 2(a)] are proportional to the spatial variations of the transmission of the mask. Similar to GI, the spatial resolution of our method is determined by the width of the autocorrelation function of the mask that modulates the input x-ray beam [44]. The autocorrelation function of the mask is presented in Fig. 2(b), while the 1D horizontal and vertical projections are presented in Figs. 2(c) and 2(d), respectively. The autocorrelation function is nearly isotropic and the FWHM of the

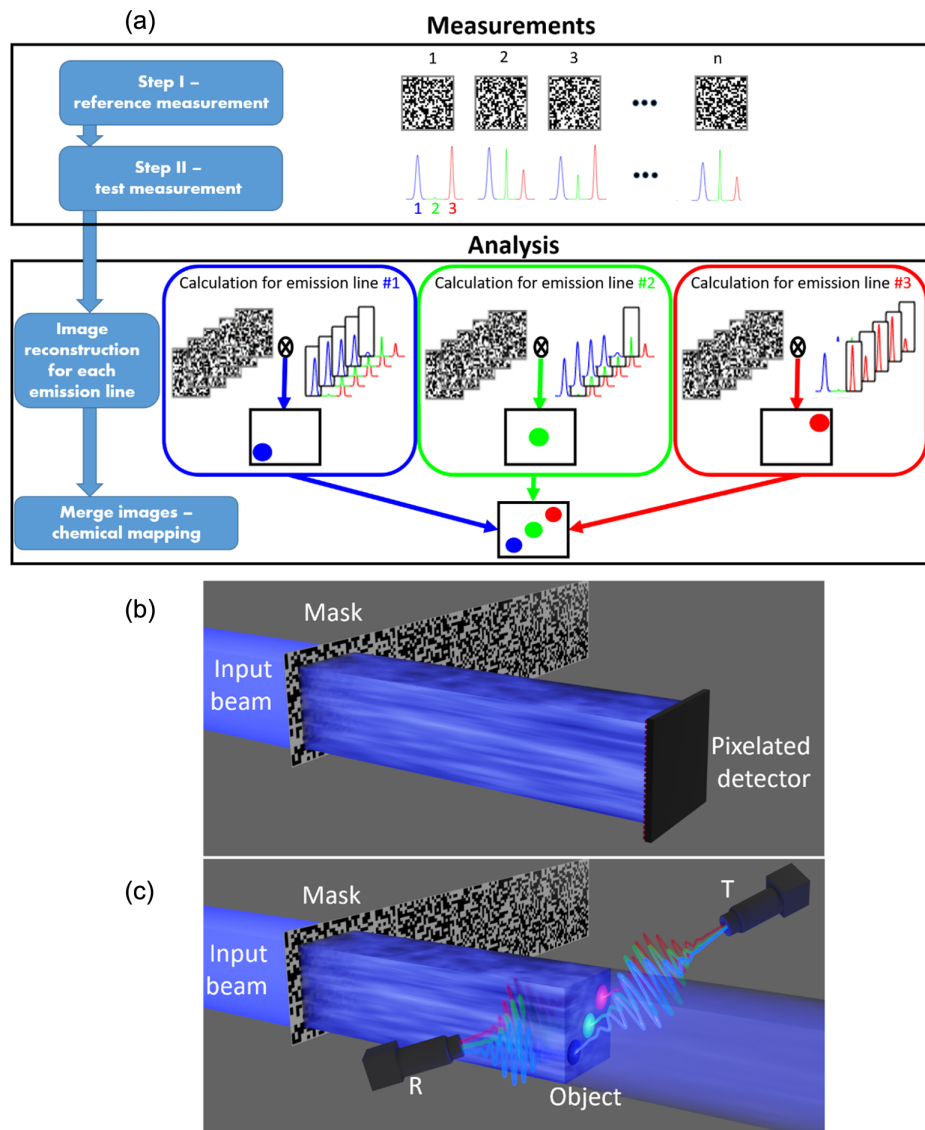


**Fig. 1.** Image reconstruction procedure and schematics of the experimental setup. (a) Flowchart of the reconstruction procedure. In Step I, we measure the intensity patterns induced by the mask in the absence of the object. In Step II we measure the fluorescence from the object. Schematics of the experimental setup for Steps I and II are shown in (b) and (c), respectively.

curve are  $33 \pm 7 \mu\text{m}$  and  $31 \pm 7 \mu\text{m}$  for the horizontal and vertical axes, respectively.

The object we imaged contains three small pieces of iron, cobalt, and brass ( $\text{Cu}_3\text{Zn}_2$ ). The direct image and the fluorescence spectrum of the objects are shown in Figs. 2(e) and 2(f), respectively.

Our method can provide the chemical map by mounting the detectors at any position around the sample and at any distance as long as they collect the fluorescence as emitted from the sample. To display this ability, we present the images reconstructed by our method for the iron and cobalt objects in Figs. 3(a) and 3(b) for detector R and detector T, respectively. The images were reconstructed using 550 realizations and the CS procedure described above. The agreement of the chemical element maps we reconstructed with the real arrangement and structures of the iron and cobalt objects is excellent and indicates the reliability of our method. The resolution of our method is clearly much higher than the spot size of our experiment that was about 1.5 mm, and we

were able to resolve the iron and cobalt objects that are separated by a gap of less than 200  $\mu\text{m}$ . In addition, we show very clearly that our method can be used to eliminate strong background noise. The images of the iron and cobalt objects are very clear, despite the strong background. Note that the copper emission lines in Fig. 2(f) are stronger than the emission lines of the iron and the cobalt by about a factor of 7. The brass object, however, could not be reconstructed because of the proximity of its emission lines to the emission lines of the radiation of our source.

After successfully showing the ability to reconstruct chemical maps with our method, we then demonstrate that we can use CS to reduce number of realizations; hence, to reduce the measurement time. To quantify the image quality of the reconstructed chemical maps we calculated the peak SNR (PSNR) as a function of the number of realizations. We plot the PSNR of the reconstructed chemical maps we measured with detector T as a function of the number of realizations in Fig. 4. The chemical maps for various compression ratios (CR) are displayed next to the graph. The CR is

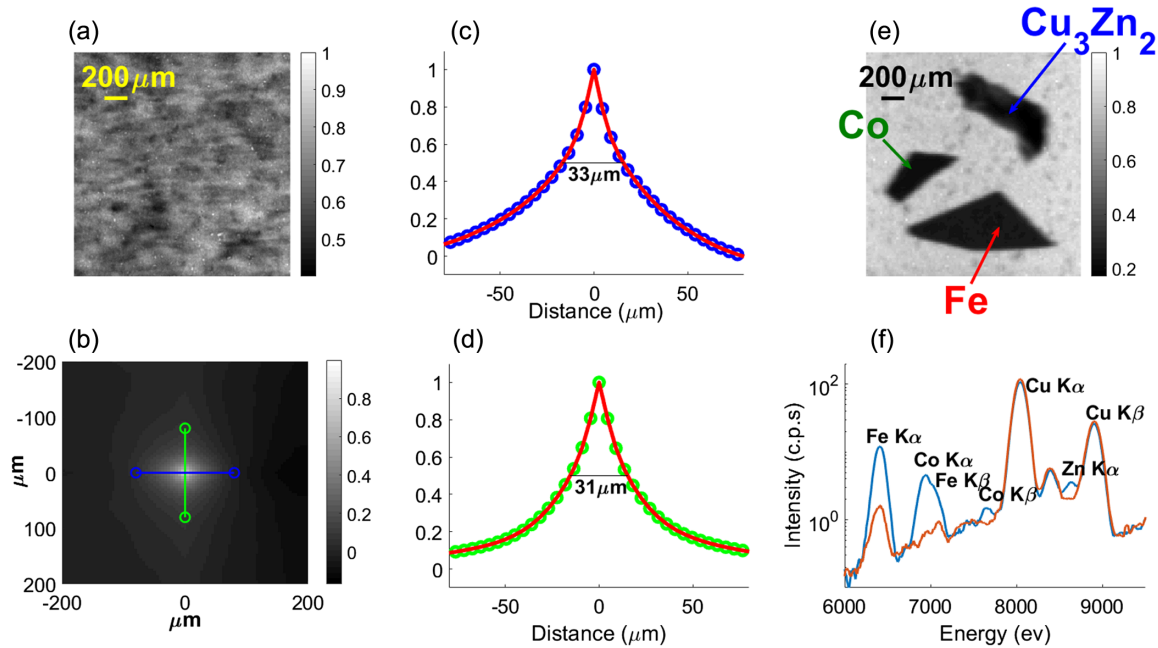


**Fig. 2.** (a) Example of the reference data (the intensity fluctuations induced by the mask). (b) Autocorrelation function of the intensity pattern induced by the mask averaged over all realizations. The blue and green lines indicate the horizontal and vertical cross sections shown in (c) and (d). The blue and green dots are the measured data for the horizontal and vertical cross sections, respectively, and the red curves are interpolation functions. In (e) and (f) normalized direct image and fluorescence spectrum of the object, which consists of iron, cobalt, and brass objects are shown. The red line is the spectrum in the absence of the sample and the blue line is the spectrum when the sample is present. The emission lines are indicated near each of the peaks.

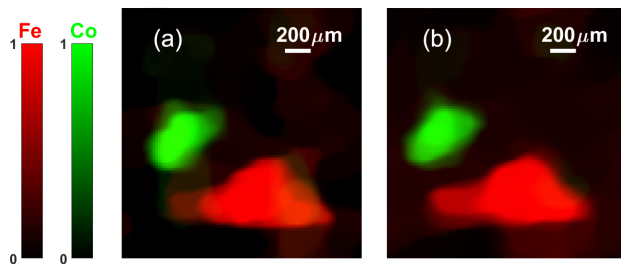


**Fig. 3.** Reconstructed chemical element maps by x-ray GF using (a) detector R and (b) detector T. The red and green areas indicate the areas containing the iron and cobalt elements, respectively.

defined by the number of pixels in the map divided by the number of realizations we used for the reconstruction [37]. The PSNR is calculated by

$$\text{PSNR} = 10 \log \left( \frac{\text{peakval}^2}{\text{MSE}} \right), \quad (3)$$

where peakval is the maximum possible pixel value of the image and MSE is the mean square error between the reconstructed image and the direct image [Fig. 2(e)]. We calculated the joint PSNR of the cobalt and the iron images as the average between the PSNR values of the images.

The maps we describe in the present work contain 1010 pixels, which is also the number of sampling points if we were using standard micro-XRF. Consequently, the CR expresses the reduction of the measurement time that our method provides. With our technique, we can see a clear image even after 144 realizations, which corresponds to a CR of 7 and identify the objects even with a CR of 20. The important consequence of this result is that with our method, the chemical maps can be measured in much shorter

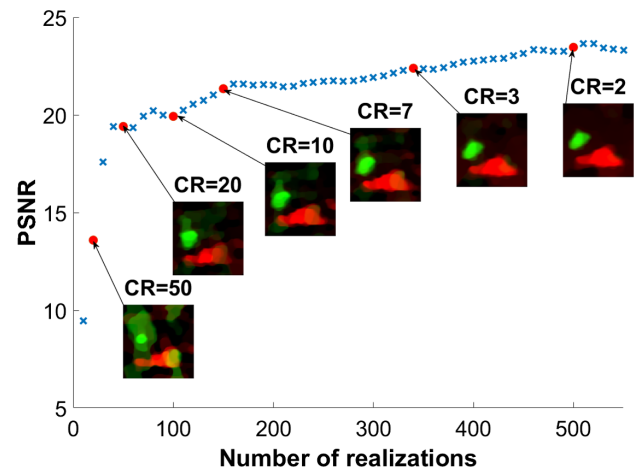


**Fig. 4.** PSNR of the reconstructed GF image measured with detector T as a function of the number of realizations. The compressive chemical element maps for various compression ratio (CR) values are displayed near the corresponding points.

times compared to standard micro-XRF methods since the number of realizations with our method is smaller than the number of sampling points with standard XRF methods.

## 4. DISCUSSION

We now discuss several important properties and implications of our method and begin with the spatial resolution. To evaluate the performance of the method and its potential to reconstruct high-spatial resolution chemical maps, we need to compare the resolutions of the reconstructed maps with the resolution of the

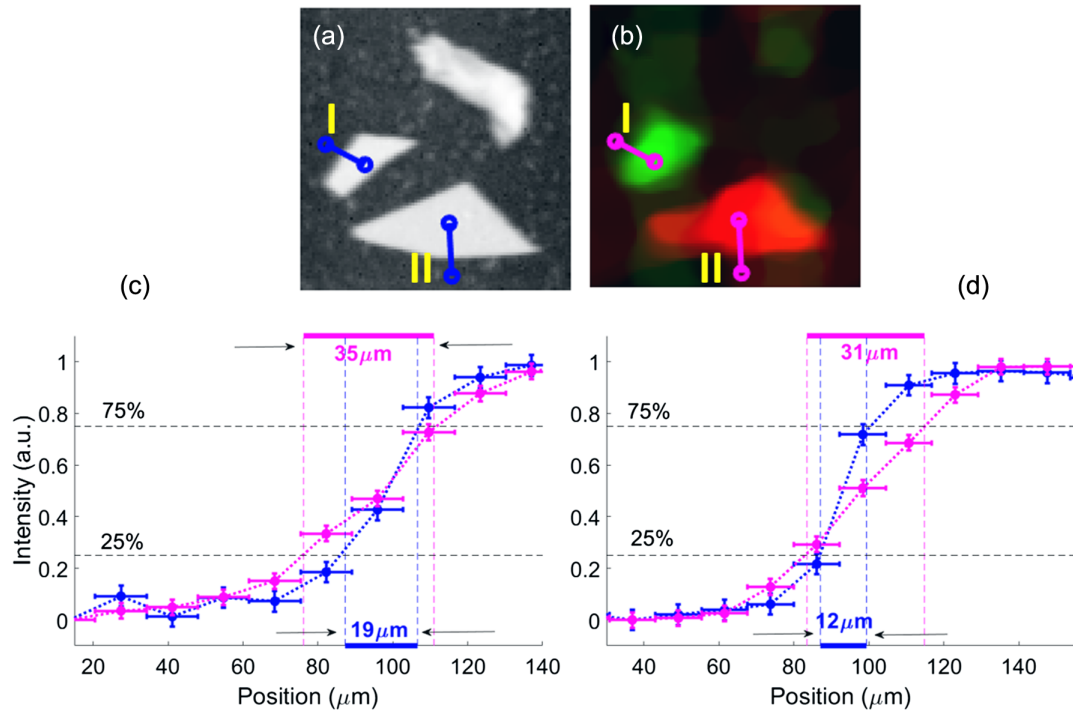


**Fig. 5.** Comparison of the resolutions of the chemical map and the direct image. Description of the edge cross sections for the (a) direct image and (b) chemical map. (c) and (d) Normalized intensity as a function of the position for cross sections I and II, respectively. The blue and magenta dots are the transmission and GF image values, respectively.

direct image of the objects and with the theoretical prediction for GF based on the measured autocorrelation function of the mask.

Since the sample we investigated includes objects with sharp edges, it is possible to estimate the resolution from the smearing of the edges. We estimate the widths of the slopes of the cross sections of the selected regions near the edges in the chemical map and compare them to the corresponding widths of the same objects in the direct image, as shown in Fig. 5. In Figs. 5(a) and 5(b), we describe the selections of the two cross sections (I and II) that are displayed for the chemical map and for the direct image, respectively. In Figs. 5(c) and 5(d), we plot the cross sections I and II, respectively. To compare to the FWHM of the correlation function, we estimated the half width of the slope of the cross sections. For the two edges presented in Fig. 5, we found that the widths of the slopes for the chemical map are  $35 \pm 7 \mu\text{m}$  and  $31 \pm 7 \mu\text{m}$  for cross sections I and II, respectively, and the corresponding widths for the direct images are  $19 \pm 7 \mu\text{m}$  and  $12 \pm 7 \mu\text{m}$ . The difference between the resolutions of the GF and the direct image exists since the resolution of GF is determined by the correlation function length of the mask, and is about  $30 \mu\text{m}$ , as we discussed above. The resolution of the direct image, however, is determined by the resolution of the pixelated detector, which is about  $15 \mu\text{m}$ . Similar results are obtained for the widths of the other edges and they are comparable, as expected, to the width of the autocorrelation function of the mask discussed above.

The resolution we demonstrated in this work is much higher than the spot size we used, which was about  $1.5 \text{ mm}$ , and it is limited by the feature sizes of the mask we used. The implication is that our method can be used for high-resolution chemical mapping at resolutions that are not limited by the focusing capabilities of a system. It is possible to improve the resolution of our method using

masks with smaller features. Recent work shows x-ray GI reconstructions with resolutions below  $10 \mu\text{m}$  using masks that were fabricated by photolithography [26,29,31] or by electroplating [26,31]. The same masks can be used for x-ray GF. Importantly, it is possible to fabricate masks with submicron features using nanotechnology techniques like e-beam lithography and x-ray photolithography. Since the feature size essentially is the parameter that controls that resolution of our method, it opens the possibility for submicron resolution XRF with tabletop sources.

Next, we consider the impact of the CS and the intensity fluctuation magnitude on the image quality since we are interested in the reduction of the measurement time with respect to standard XRF methods, but without deteriorating the image quality. While a high CR can lead to significant reduction in the measurement time it may reduce the image quality and, as we show below, the quality also depends on the magnitude of the intensity fluctuations. Because the image quality in GI methods is determined by the ratio between the variations of the detected intensities for the different realizations to the noise, we define the fluctuation-to-noise ratio (FNR) as

$$\text{FNR} = \frac{\text{std}(s)}{\langle \sqrt{s} \rangle}, \quad (4)$$

where  $s$  is the set of the intensities detected at a specific emission line during entire measurement,  $\langle \cdot \rangle$  is the average over all realizations, and  $\text{std}$  is the standard deviation.

We simulated the experiment and calculated the PSNR of the reconstructed cobalt and iron images as function of the FNR for reconstructed CRs. In Fig. 6, we show the results of our simulations. The solid lines are the corresponding fitting curves that we added as guides for the eye. From the results presented in Fig. 6, we see that for FNRs below 1, the PSNR is very small. These values indicate, as

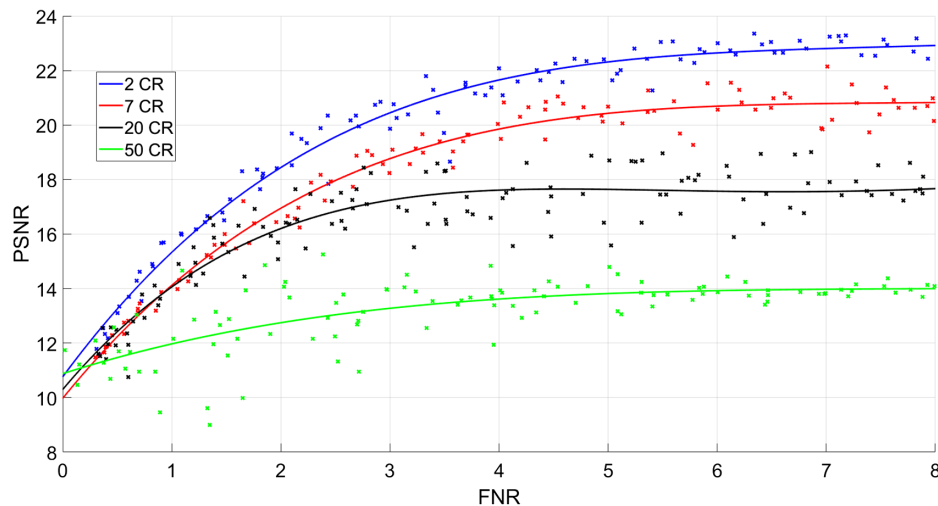


**Fig. 6.** Dependence of the reconstruction quality of the chemical map on the CR and FNR. The points are the simulation results, and the lines are the corresponding fitting curves to show the trend of the results. See further details in the article.

expected, that no clear image can be reconstructed for FNR values below 1. As the FNR increases, the image quality improves until the value is about 5. At higher FNR values, the image quality is nearly independent from the FNR for any CS value.

For the parameters in our experiment, the FNR values are 3.4 and 4.8 for the cobalt and iron objects, respectively, and the average is 4.1. Accordingly, the PSNR is about 23 for the CR of 2, as shown in Fig. 4. The simulations also explain why we could reconstruct the iron and cobalt, but not the brass object. The brass contains copper and zinc with emission lines very close to the characteristic emission lines of our source, as can be clearly seen in Fig. 2(f), which suggests that the data are noisy for brass. However, it is still possible to resolve the zinc  $K_{\alpha}$  line, which might indicate the possibility to reconstruct the brass with standard XRF methods. The FNR, however, is only 1.8, which prevents the reconstruction by GF. This can be overcome in the future by choosing well-separated emission lines or by increasing the depth of the mask features.

From Fig. 6 and the discussion above, it is clear that the reconstruction quality depends on the FNR and the CR. We still, however, need to discuss the impact of the FNR on the reduction of the measurement time and to compare it to the raster scan XRF. In this work, we demonstrated a reduction of the measurement time as the result of reducing the number of scanning points, which is enabled by CS. To understand the reduction in the measurement time compared to standard XRF measurements, we recall that for standard XRF the measurement time is limited by the requirement for sufficient SNR; thus, it depends on the flux of the radiation that irradiates the sample. Since the FNR cannot exceed the SNR, the measurement time of GF will not be shorter than the measurement time of standard methods unless a priori knowledge on the object is used. However, in most cases, there is a priori information such as the sparsity of the object that is used for the application of CS. It is used to reduce the measurement time of GF, as we demonstrated in the present work. Therefore, the measurement time with GF would be shorter than standard methods if the gain using a priori knowledge is larger than the deterioration of the image quality caused by the difference between the SNR and the FNR [42,45,46]. It is clear that when the measurement duration per measurement point (a single sample position for raster scan and a single realization for GF) is not limited by the shot noise (for

example, when the motor speed is the limitation), our approach is advantageous, since both the SNR and the FNR can be very high. Hence, the application of CS reduces the number of measurement points and therefore the measurement time.

Finally, we note that since the aspect ratio of the mask features is limited by fabrication or by physical constraints and since the lateral size of the mask features controls the spatial resolution, there is a tradeoff between the resolution and the FNR. This constraint has an important impact on the image quality and on the ability to reduce the measurement time.

## 5. CONCLUSION

Our work opens the possibility to develop a fast high-resolution chemical element mapping technique without focusing and without moving the sample. In addition to a reduced cost and improved mechanical stability, our method has several advantages over standard methods, which includes a smaller number of sampling points and the applicability for a broad range of photon energies. Further generalization of our results will lead to new applications to extend the capabilities and the impact of XRF to new areas. Medical imaging, for example, can benefit from our method because it is performed at photon energies where lenses are not practical and where the low contrast between various tissues is the main challenge. Today, to improve the visibility and quality of images of soft tissues, contrast agents are used since their transmission contrast is higher than the transmission contrast between different types of soft tissues. However, even with the contrast agents, the visibility is limited. A potential further development of our method is for the measurement the fluorescence from the same contrast agents as a complementary or a completely new modality that could increase the quality of the images or alternatively reduce the dose of the measurements since the fluorescence contrast is significantly higher than the transmission contrast. Another example is for full body scanners used for national security applications. Since our method can provide element-specific images and can be tuned to be blind to human tissues, it can be used to improve the privacy protection of inspected passengers in contrast to other x-ray modalities. Finally, we point out that it is possible to replace the input x-ray beam with an electron beam to excite the inner

shell electrons [47]. In this case, spatial resolutions that exceeds the nanometer scale are feasible and, with our method, it will be possible to significantly reduce the scanning duration.

**Funding.** Israel Science Foundation (847/21).

**Acknowledgment.** Author Yishay Klein gratefully acknowledges the support of the Ministry of Science & Technologies, Israel.

**Disclosures.** The authors declare no conflicts of interest.

**Data Availability.** All data are available in the main text or in Supplement 1. Codes are available upon request from the authors.

**Supplemental document.** See Supplement 1 for supporting content.

## REFERENCES

- J. Lim, Y. Li, D. H. Alsem, H. So, S. C. Lee, P. Bai, D. A. Cogswell, X. Liu, N. Jin, Y. Yu, N. J. Salmon, D. A. Shapiro, M. Z. Bazant, T. Tylliszczak, and W. C. Chueh, "Origin and hysteresis of lithium compositional spatiodynamics within battery primary particles," *Science* **353**, 566–571 (2016).
- A. Cvetkovic, A. L. Menon, M. P. Thorgersen, J. W. Scott, F. L. Poole, II, F. E. Jenney, Jr., W. A. Lancaster, J. L. Praissman, S. Shanmukh, B. J. Vaccaro, S. A. Trauger, E. Kalisiak, J. V. Apon, G. Siuzdak, S. M. Yannoni, J. A. Tainer, and M. W. W. Adams, "Microbial metalloproteomes are largely uncharacterized," *Nature* **466**, 779–782 (2010).
- R. A. Wogelius, P. L. Manning, H. E. Barden, N. P. Edwards, S. M. Webb, W. I. Sellers, K. G. Taylor, P. L. Larson, P. Dodson, H. You, L. Da-Qing, and U. Bergmann, "Trace metals as biomarkers for eumelanin pigment in the fossil record," *Science* **333**, 1622–1626 (2011).
- A. C. Allwood, M. T. Rosing, D. T. Flannery, J. A. Hurowitz, and C. M. Heirweh, "Reassessing evidence of life in 3,700-million-year-old rocks of Greenland," *Nature* **563**, 241–244 (2018).
- SPECTRO Analytical Instruments GmbH, "High-precision analysis of small parts for aerospace and automotive applications," <https://extranet.spectro.com/-/media/21264D4E-0D97-490B-996F-9E3C59CADBE6.pdf>.
- R. Ploeger and A. Shugar, "Where science meets art," *Science* **354**, 826–828 (2016).
- G. E. Ice, J. D. Budai, and J. W. L. Pang, "The race to x-ray microbeam and nanobeam science," *Science* **334**, 1234–1239 (2011).
- B. Golosio, A. Simionovici, A. Somogyi, L. Lemelle, M. Chukalina, and A. Brunetti, "Internal elemental microanalysis combining x-ray fluorescence, Compton and transmission tomography," *J. Appl. Phys.* **94**, 145–156 (2003).
- S. A. Kim, T. Punshon, A. Lanzirotti, L. Li, J. M. Alonso, J. R. Ecker, J. Kaplan, and M. Lou Gueriot, "Localization of iron in arabidopsis seed requires the vacuolar membrane transporter VIT1," *Science* **314**, 1295–1298 (2006).
- S. Bauters, P. Tack, J. H. Rudloff-Grund, D. Banerjee, A. Longo, B. Vekemans, W. Bras, F. E. Brenker, R. van Silfhout, and L. Vincze, "Polycapillary optics based confocal micro x-ray fluorescence and x-ray absorption spectroscopy setup at the European synchrotron radiation facility collaborative research group Dutch–Belgian beamline, BM26A," *Anal. Chem.* **90**, 2389–2394 (2018).
- G. Chen, S. Chu, T. Sun, X. Sun, L. Zheng, P. An, J. Zhu, S. Wu, Y. Du, and J. Zhang, "Confocal depth-resolved fluorescence micro-x-ray absorption spectroscopy for the study of cultural heritage materials: a new mobile endstation at the Beijing Synchrotron Radiation Facility," *J. Synchrotron Radiat.* **24**, 1000–1005 (2017).
- K. Tsuji, T. Matsuno, Y. Takimoto, M. Yamanashi, N. Kometani, Y. C. Sasaki, T. Hasegawa, S. Kato, T. Yamada, T. Shoji, and N. Kawahara, "New developments of x-ray fluorescence imaging techniques in laboratory," *Spectrochim. Acta B At. Spectrosc.* **113**, 43–53 (2015).
- G. Xiong, W. Jia, Q. Shan, X. Zhang, X. Tang, and J. Li, "Equipment design and performance characterization of full field x-ray fluorescence (FF-XRF) element distribution imaging system with combined collimating lens (CCL)," *Rev. Sci. Instrum.* **91**, 123701 (2020).
- A. Kulow, A. G. Buzanich, U. Reinholz, C. Strelli, and M. Radtke, "On the way to full-field x-ray fluorescence spectroscopy imaging with coded apertures," *J. Anal. At. Spectrom.* **35**, 347–356 (2020).
- A. Haboub, A. A. MacDowell, S. Marchesini, and D. Y. Parkinson, "Coded aperture imaging for fluorescent x-rays," *Rev. Sci. Instrum.* **85**, 063704 (2014).
- B. De Samber, O. Scharf, G. Buzanich, J. Garrevoet, P. Tack, M. Radtke, H. Riesemeier, U. Reinholz, R. Evens, K. De Schampelaere, G. Falkenberg, C. Janssen, and L. Vincze, "Three-dimensional x-ray fluorescence imaging modes for biological specimens using a full-field energy dispersive CCD camera," *J. Anal. At. Spectrom.* **34**, 2083–2093 (2019).
- J. R. Betterton, D. Ratner, S. Webb, and M. Kochenderfer, "Reinforcement learning for adaptive illumination with x-rays," in *Proceedings—IEEE International Conference on Robotics and Automation* (2020).
- K. Hwang, Y. H. Seo, J. Ahn, P. Kim, and K. H. Jeong, "Frequency selection rule for high definition and high frame rate Lissajous scanning," *Sci. Rep.* **7**, 14075 (2017).
- M. M. Noack, K. G. Yager, M. Fukuto, G. S. Doerk, R. Li, and J. A. Sethian, "A Kriging-based approach to autonomous experimentation with applications to x-ray scattering," *Sci. Rep.* **9**, 11809 (2019).
- J. H. Shapiro, "Computational ghost imaging," *Phys. Rev. A* **78**, 061802 (2008).
- G. M. Gibson, S. D. Johnson, and M. J. Padgett, "Single-pixel imaging 12 years on: a review," *Opt. Express* **28**, 28190–28208 (2020).
- M. Lyu, W. Wang, H. Wang, H. Wang, G. Li, N. Chen, and G. Situ, "Deep-learning-based ghost imaging," *Sci. Rep.* **7**, 17865 (2017).
- R. Baraniuk and P. Steeghs, "Compressive radar imaging," in *IEEE Radar Conference* (IEEE, 2007), pp. 128–133.
- H.-C. Liu and S. Zhang, "Computational ghost imaging of hot objects in long-wave infrared range," *Appl. Phys. Lett.* **111**, 031110 (2017).
- D. Shrekenhamer, C. M. Watts, and W. J. Padilla, "Terahertz single pixel imaging with an optically controlled dynamic spatial light modulator," *Opt. Express* **21**, 12507–12518 (2013).
- Y. H. He, A. X. Zhang, M. F. Li, Y. Y. Huang, B. G. Quan, D. Z. Li, L. A. Wu, and L. M. Chen, "High-resolution sub-sampling incoherent x-ray imaging with a single-pixel detector," *APL Photon.* **5**, 056102 (2020).
- V. Studer, J. Bobin, M. Chahid, H. S. Mousavi, E. Candes, and M. Dahan, "Compressive fluorescence microscopy for biological and hyperspectral imaging," *Proc. Natl. Acad. Sci. USA* **109**, E1679–E1687 (2012).
- B. Sun, M. P. Edgar, R. Bowman, L. E. Vittert, S. Welsh, A. Bowman, and M. J. Padgett, "3D computational imaging with single-pixel detectors," *Science* **340**, 844–847 (2013).
- Y. Klein, A. Schori, I. P. Dolbnya, K. Sawhney, and S. Schwartz, "X-ray computational ghost imaging with single-pixel detector," *Opt. Express* **27**, 3284–3293 (2019).
- O. Sefi, Y. Klein, E. Strizhevsky, I. P. Dolbnya, and S. Schwartz, "X-ray imaging of fast dynamics with single-pixel detector," *Opt. Express* **28**, 24568–24576 (2020).
- Y.-H. He, A.-X. Zhang, W.-K. Yu, L.-M. Chen, and L.-A. Wu, "Energy-selective x-ray ghost imaging," *Chin. Phys. Lett.* **37**, 044208 (2020).
- A.-X. Zhang, Y.-H. He, L.-A. Wu, L.-M. Chen, and B.-B. Wang, "Tabletop x-ray ghost imaging with ultra-low radiation," *Optica* **5**, 374–377 (2018).
- S. Ota, R. Horisaki, Y. Kawamura, M. Ugawa, I. Sato, K. Hashimoto, R. Kamesawa, K. Setoyama, S. Yamaguchi, K. Fujiu, K. Waki, and H. Noji, "Ghost cytometry," *Science* **360**, 1246–1251 (2018).
- N. Tian, Q. Guo, A. Wang, D. Xu, and L. Fu, "Fluorescence ghost imaging with pseudothermal light," *Opt. Lett.* **36**, 3302–3304 (2011).
- O. Katz, Y. Bromberg, and Y. Silberberg, "Compressive ghost imaging," *Appl. Phys. Lett.* **95**, 131110 (2009).
- A. M. Kingston, G. R. Myers, D. Pelliccia, F. Salvemini, J. J. Bevitt, U. Garbe, and D. M. Paganin, "Neutron ghost imaging," *Phys. Rev. A* **101**, 053844 (2020).
- S. Li, F. Cropp, K. Kabra, T. J. Lane, G. Wetzstein, P. Musumeci, and D. Ratner, "Electron ghost imaging," *Phys. Rev. Lett.* **121**, 114801 (2018).
- D. Pelliccia, A. Rack, M. Scheel, V. Cantelli, and D. M. Paganin, "Experimental x-ray ghost imaging," *Phys. Rev. Lett.* **117**, 113902 (2016).
- A. Schori and S. Schwartz, "X-ray ghost imaging with a laboratory source," *Opt. Express* **25**, 14822–14828 (2017).
- H. Yu, R. Lu, S. Han, H. Xie, G. Du, T. Xiao, and D. Zhu, "Fourier-transform ghost imaging with hard x rays," *Phys. Rev. Lett.* **117**, 113901 (2016).
- A. Schori, D. Borodin, K. Tamasaku, and S. Schwartz, "Ghost imaging with paired x-ray photons," *Phys. Rev. A* **97**, 063804 (2018).

42. T. J. Lane and D. Ratner, "What are the advantages of ghost imaging? Multiplexing for x-ray and electron imaging," *Opt. Express* **28**, 5898–5918 (2020).
43. C. Li, W. Yin, H. Jiang, and Y. Zhang, "An efficient augmented Lagrangian method with applications to total variation minimization," *Comput. Optim. Appl.* **56**, 507–530 (2013).
44. A. Gatti, E. Brambilla, M. Bache, and L. A. Lugiato, "Ghost imaging with thermal light: comparing entanglement and classical correlation," *Phys. Rev. Lett.* **93**, 093602 (2004).
45. A. M. Kingston, W. K. Fullagar, G. R. Myers, D. Adams, D. Pelliccia, and D. M. Paganin, "Inherent dose-reduction potential of classical ghost imaging," *Phys. Rev. A* **103**, 033503 (2021).
46. D. Ceddia and D. M. Paganin, "Random-matrix bases, ghost imaging, and x-ray phase contrast computational ghost imaging," *Phys. Rev. A* **97**, 062119 (2018).
47. X. Llovet, A. Moy, P. T. Pinard, and J. H. Fournelle, "Electron probe micro-analysis: A review of recent developments and applications in materials science and engineering," *Prog. Mater. Sci.* **116**, 100673 (2021).